High-stability optical clock based on a continuously ground-state cooled Al^+ ion without compromising its accuracy

Fabian Dawel,[1,2] Lennart Pelzer,[1] Kai Dietze,[1,2] Johannes Kramer,[1,2] Marek Hild,[1] Steven A. King,[1,*] Nicolas C. H. Spethmann,[1] Joshua Klose,[1] Kilian Stahl,[1] Sören Dörscher,[1] Erik Benkler,[1] Christian Lisdat,[1] Sergey G. Porsev,[3] Marianna S. Safronova,[3,†] and Piet O. Schmidt[1,2,‡]

[1]*Physikalisch-Technische Bundesanstalt, Bundesallee 100, 38116 Braunschweig, Germany*

[2]*Institut für Quantenoptik, Leibniz Universität Hannover, Welfengarten 1, 30167 Hannover, Germany*

[3]*Department of Physics and Astronomy, University of Delaware, Newark, Delaware 19716, USA*

(Received 4 November 2025; accepted 27 April 2026; published 23 June 2026)

Single-ion optical clocks have shown systematic frequency uncertainties below 10^{-18}, but typically require more than one week of averaging to achieve a corresponding statistical uncertainty. This time can be reduced with longer probe times, but comes at the cost of a higher time-dilation shift due to motional heating of the ions in the trap. We show that sympathetic ground-state cooling using electromagnetically induced transparency of an Al^+ clock ion via a cotrapped Ca^+ ion during clock interrogation suppresses the heating of the ions. Al^+ can be kept close to the motional ground state, independent from the chosen interrogation time, at a relative time-dilation shift of $(-1.69 \pm 0.20) \times 10^{-18}$. The Ca^+ cooling light introduces an additional light shift on the Al^+ clock transition of $(-9.3 \pm 1.1) \times 10^{-18}$. We project that the uncertainty of this light shift can be further reduced by nearly an order of magnitude. This sympathetic cooling enables seconds of interrogation time with 10^{-19} motional and cooling laser-induced uncertainties for Al^+ and can be employed in other ion clocks as well.

DOI: 10.1103/48zr-2t1p

I. INTRODUCTION

Optical clocks are the most accurate measurement devices, reaching estimated relative systematic frequency uncertainties in the 10^{-19} regime [1–4]. Frequency ratios between optical clocks have been measured down to an uncertainty level of a few 10^{-18} [5–10]. This level of precision can be used for measuring centimeter height differences in relativistic geodesy [11–14], to set improved bounds on variation of fundamental constants and dark matter candidates [10,15–20], or test relativity [6,7,21]. All these applications benefit from fast averaging times to achieve a certain precision: In relativistic geodesy and tests of relativity, dynamic changes could be resolved as the Earth is rotating; in the search for dark matter, the mass range of dark matter candidates can be extended toward heavier masses.

While neutral atom lattice clocks probe hundreds to thousands of atoms at a time, ion clocks are currently restricted to one or a few ions, limiting their signal-to-noise ratio [22] and thus requiring long averaging times.

The stability of clocks is fundamentally limited by quantum projection noise (QPN) [23]. The statistical uncertainty, expressed in the form of an Allan deviation for a clock probing N_{at} atoms using Ramsey interrogation and averaging for a time τ, is given by [24,25]

$$\sigma_y(\tau) \approx C \frac{\Delta\nu}{\nu_0} \sqrt{\frac{t_c}{N_{\mathrm{at}}\tau}}, \tag{1}$$

where C is a constant on the order of 1, $\Delta\nu$ is the Ramsey fringe width, ν_0 is the transition frequency, and t_c is the time of one complete clock cycle. Single-ion clocks typically achieve a stability of $10^{-15}/\sqrt{\tau/1\,\mathrm{s}}$ [6,10]. To improve the ion clock stability, one can use multiple ions to increase the amount of signal per cycle [8,26–30], or longer interrogation times to reduce $\Delta\nu$. The maximum interrogation time is ultimately limited by the excited state lifetime of the clock transition or by the laser coherence time [31]. The former is a fundamental limitation, while the latter can be improved by better clock lasers [32] or compound clocks [33–35] that use additional atomic ensembles for prestabilization of the laser.

Another limitation to long probe times in ion clocks is the second-order Doppler or time-dilation shift [22,36] arising from residual thermal motion of the ion. It depends on the average kinetic energy during the probe time, which increases with time due to motional heating of the ion. The responsible heating rates depend on the size and type of the used trap with reported heating rates of $1-10^4$ phonons/s for room temperature setups [37]. The determination of the resulting kinetic energy is model dependent and the heating rate can change

*Present address: Oxford Ionics, Oxford OX5 1GN, United Kingdom.

†Contact author: msafrono@udel.edu

‡Contact author: Piet.Schmidt@quantummetrology.de

Published by the American Physical Society under the terms of the Creative Commons Attribution 4.0 International license. Further distribution of this work must maintain attribution to the author(s) and the published article's title, journal citation, and DOI.

with environmental disturbances, complicating the systematic shift analysis [1,38–41]. Furthermore, motional heating can lead to thermal dephasing for long probe times, resulting in a reduced contrast C [42] and thus reduced stability according to Eq. (1).

Cooling during interrogation ensures that the ion motion is in a steady state. This eliminates the effect of the heating rate on the second-order Doppler shift. Several two-ion species experiments implemented Doppler cooling during clock interrogation [3,41,43,44]. The Doppler cooling rate is typically much larger than the heating rates and will keep the ion at the Doppler temperature. Here, we go one step further and use electromagnetically induced transparency (EIT) cooling, since it can reach the motional ground state [45,46] while still cooling all modes at once [47,48]. The advantage of EIT cooling over Doppler cooling is the achievable lower mean motional quantum number, resulting in an order of magnitude smaller time-dilation shift. This significantly simplifies characterization of this shift, which otherwise requires careful calibration [3,49]. We demonstrate that the systematic frequency uncertainty associated with the ac-Stark shift induced by the cooling lasers is compatible with clock operation at the 10^{-18} level and below.

II. SETUP

Our experimental setup is described in Refs. [47,50]. In short, we use a linear Paul trap, consisting of four blades and two end-cap electrodes, as well as two additional electrodes for micromotion compensation. The distance between the blades is 1.6 mm and the distance between the end caps is 5 mm. We drive the trap blade pairs with near-equal amplitude at an rf drive frequency of 28 MHz, resulting in single Ca^+ trap frequencies of $(\omega_x, \omega_y, \omega_z) = (1.95, 1.85, 1.1)$ MHz, where z is the axial direction. Figure 1 illustrates the cooling and clock laser directions relative to the trap. The intensities of all cooling lasers involved are measured via photodiodes before the vacuum chamber. These voltages are used for an intensity stabilization of the laser light via a digital sample and hold circuitry. The trap is inside a stainless-steel vacuum chamber at room temperature with a pressure of 11(6) nPa, measured via swapping rates of an Al^+-Ca^+ crystal [51]. The magnetic field of 0.15 mT along the trap axis is generated by two external coils. We use an additional set of coils for active magnetic field stabilization to reduce magnetic field drift and noise, mainly at 50 Hz. With the magnetic field stabilization, we measure on the $S_{1/2}(m = -1/2) \leftrightarrow D_{5/2}(m = -1/2)$ coherence times of around 1 ms.

For EIT cooling, we use 397 nm π- and σ^--polarized light. Here, σ^- is the strong pump beam, while π is the probe beam. These beams have an effective wave vector that overlaps with all motional modes of the crystal (see also Fig. 1). We use a common blue detuning of 64(4) MHz, limited by the available laser power [52]. To cool all modes at once, we set the light shift of the σ^- EIT beam to a value of 2.3 MHz, which maximizes the cooling efficiency of modes around this motional frequency. We use 10 ms of precooling before clock interrogation to establish a steady state of the mean motional mode occupation.

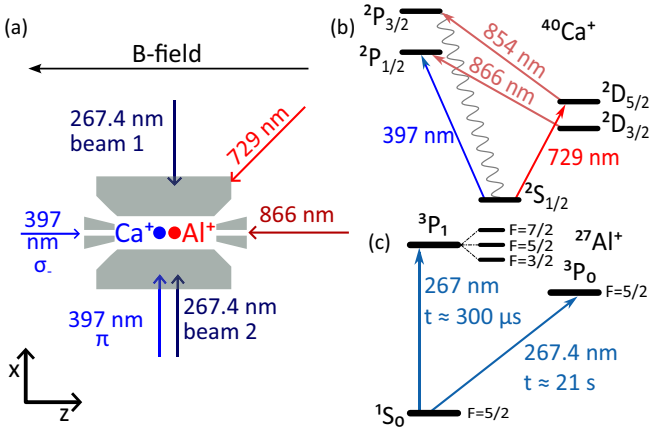


FIG. 1. (a) Laser setup around the trap, showing cooling and clock lasers. Compensation of the first-order Doppler shift is realized with two counterpropagating clock laser beams. For cooling of the Al^+-Ca^+ crystal, we use 397 nm σ^- and π beams and a repump 866 nm beam. The σ^- and repump beams are aligned along the trap axis. The 397 nm π beam is perpendicular to the trap axis, as well as the clock laser. For motional sideband spectroscopy via Ca^+, the 729 nm laser is aligned with an angle of around 45° to the trap axis in the xz plane, such that it can address all motional modes. Panels (b) and (c) show partial level schemes of Ca^+ and Al^+, respectively.

The clock is interrogated by probing the stretched states of the $^1S_0 \leftrightarrow {}^3P_0$ transition of Al^+, to eliminate the first-order Zeeman shift. The Zeeman states are prepared through frequency-addressed optical pumping on the Al^+ $^1S_0 \leftrightarrow {}^3P_0$ transition. The interrogation order between the states is randomized. The clock state is read out via a repeated quantum nondemolition measurement protocol [53].

Long coherence times are achieved by frequency locking the clock laser at its second subharmonic at 1069 nm to a high-finesse cavity [54] and transfer lock [55] it to a laser with a relative frequency stability noise floor of 4×10^{-17} [32] using the end-to-end topology to minimize differential optical path length fluctuations [56]. All fiber paths are length stabilized using acousto-optic modulators [57]. We use two second harmonic generation stages with similar path length stabilization in between, resulting in a stability of below $1 \times 10^{-16}/\sqrt{\tau/1\,\mathrm{s}}$ directly after the last doubling system [58]. Using length-stabilized UV fibers [59,60], we bring the light near the vacuum chamber, leaving an uncompensated free-space path of around 40 cm to the ion. For the clock interrogation, we use Ramsey spectroscopy with 250 ms dark time and 25 ms pulse duration per pulse. The dead time is around 40% of the overall clock cycle. The EIT cooling and repump lasers are on during the complete clock interrogation.

III. STABILITY MEASUREMENT

We measured the stability of the frequency ratio of the $^{27}Al^+$ clock against an ^{87}Sr-optical lattice clock [8,61], as shown in Fig. 2. When the statistical uncertainty of the Sr-lattice clock of $1.1 \times 10^{-16}/\sqrt{\tau/1\,\mathrm{s}}$ is subtracted from the fitted value, we obtain a frequency stability of $6.0 \times 10^{-16}/\sqrt{\tau/1\,\mathrm{s}}$ for Al^+. This is in agreement with a quantum projection noise-limited measurement with a contrast of 93%. The result confirms that statistical fluctuations from the

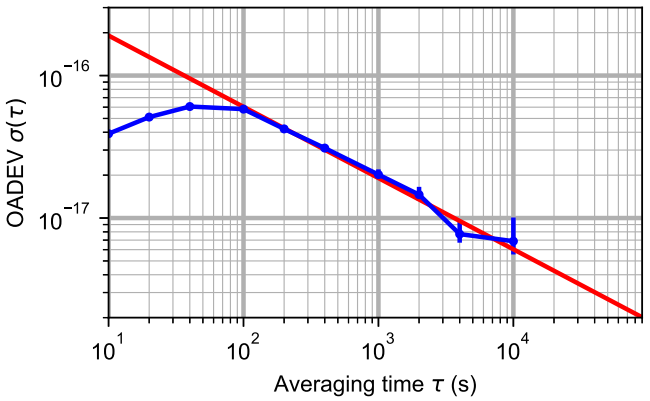


FIG. 2. Stability measurement of the frequency ratio between ^{87}Sr and $^{27}Al^+$ (blue dots). The red line is a fit to the white frequency noise regime with a resulting stability of $6.1 \times 10^{-16}\sqrt{\tau/1\,\mathrm{s}}$. This measurement data are concatenated from multiple shorter runs during one week.

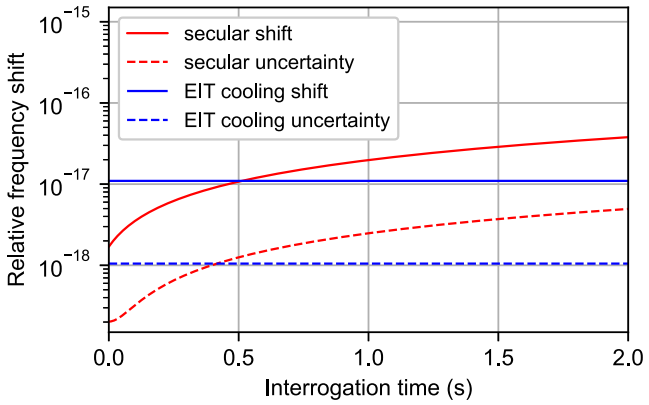


FIG. 3. Frequency shift vs interrogation time. The frequency shift includes the measured time-dilation shift and the ac-Stark shift of the cooling lasers. With EIT cooling the shift is stationary, while the shift increases without cooling due to motional heating. For a lifetime-limited interrogation of 21 s, the shift increases up to $(3.77 \pm 0.51) \times 10^{-16}$.

presence of the cooling laser are absent down to a level of 6×10^{-18} fractional frequency uncertainty.

IV. SECOND-ORDER DOPPLER SHIFT

While simultaneous cooling allows long probe times and therefore improves the statistical frequency uncertainty, we need to evaluate the systematic frequency shifts from residual secular motion and the cooling laser-induced ac-Stark shift on the Al^+ clock transition (see Fig. 3). The secular kinetic energy is determined from the mean motional state occupation and the normal mode frequencies (for details, see Appendix A). Secular frequencies are measured via the $S_{1/2} \rightarrow D_{5/2}$ transition in Ca^+ in the resolved sideband regime. Measuring the mean motional state occupation relies on knowing the underlying state distribution, which changes depending on the cooling technique. Resolved sideband cooling generates a state distribution that can be approximated by a double-thermal distribution [49], while Doppler cooling [62] and EIT cooling yield a thermal distribution [46]. We employ the sideband thermometry method to obtain the mean motional state, predicated on the presence of the expected thermal distribution [62].

We measured the excitation probability ratio between blue and red sidebands for all axial and radial out-of-phase modes for times of up to 250 ms of cooling, confirming that the mean motional state occupation is stable over the probe time. The ratio for the radial in-phase modes is inferred from frequency scans over the respective sideband for up to 80 ms. This is necessary due to weak coupling (see Table I) and a frequency drift of the sidebands. The drift is presumably due to thermal changes of the helical resonator driving the trap rf electrodes, which slightly change the resonance frequency. We also confirmed that the cooling performance is independent of the ion crystal ordering.

The advantage of EIT over Doppler cooling becomes evident from the measured mean motional quantum numbers, $\bar{n}$, shown in Table I: all modes are cooled well below the Doppler limit, resulting in an overall motional shift and associated uncertainty of $(-1.69 \pm 0.20) \times 10^{-18}$, which is smaller compared to Doppler cooling [3]. The axial

TABLE I. Motional mode parameters of an Al^+-Ca^+ crystal. Here, ω is the motional mode frequency, b_i are the normalized eigenvector components of aluminum, η_{729} is the Lamb-Dicke parameter of the 729 nm laser on Ca^+ (which includes the projection of the laser on the mode), and S is the multiplicative contribution due to intrinsic micromotion. The mean motional state after Doppler and EIT cooling is given by $\bar{n}_{\mathrm{Dop}}$ (calculated) and $\bar{n}_{\mathrm{EIT}}$ (measured), respectively. The heating rate is $\dot{\bar{n}}$. The time-dilation shift (TDS) with cooling column shows the resulting frequency shift of each mode for the measured $\bar{n}_{\mathrm{EIT}}$. The radial (rad) in-phase (ip) mode and the axial (ax) out-of-phase (op) mode have the largest weight for the secular motional shift on Al^+, which is shown in the next-to-last column. The last column shows the shift per time when no cooling is applied during the interrogation. In the last two columns, we neglect the zero-point energy.

Mode	ω (MHz)	b_m	S	η_{729}	$\bar{n}_{\mathrm{Dop}}$	$\bar{n}_{\mathrm{EIT}}$	TDS with cooling (10^{-18})	$\dot{\bar{n}}$ (quantum/s)	shift/quantum (10^{-19})	shift/time (10^{-18} t/s)
ax ip	1.25	0.562	0	0.051	9.9	1.1(4)	0.054(15)	56(6)	0.33	0.97(10)
ax op	2.26	0.827	0	0.026	5.5	0.11(5)	0.077(6)	3.7(1.0)	1.27	0.31(6)
rad x op	1.759	0.157	3.17	0.039	7.0	0.35(8)	0.00125(12)	37(4)	0.15	0.28(3)
rad y op	1.766	0.157	3.17	0.030	7.0	0.18(4)	0.00101(7)	7.8(1.3)	0.15	0.07(1)
rad x ip	2.868	0.988	1.21	0.005	4.3	0.78(19)	0.66(10)	53(8)	5.2	14.4(2.1)
rad y ip	2.912	0.988	1.21	0.004	4.3	1.18(34)	0.88(18)	11(5)	5.2	3.7(1.3)

out-of-phase mode is most efficiently cooled, since it is closest to the optimal EIT cooling condition.

V. ac-STARK SHIFT

A downside of cooling during interrogation is the differential ac-Stark shift of the cooling lasers on the clock transition. The three light beams that cause a shift are the 397 nm π and σ^- beams and the 866 nm repump beam. To estimate the light shift on the clock transition $\Delta\nu_c$, we need to know the differential polarizability of the clock transition of Al^+, $\Delta\alpha$, and the electric field $E(t) = E_0\cos(\omega t)$ of the cooling beams. The former is extrapolated from polarizability measurements in the infrared wavelength regime, while the latter is derived from the ac-Stark shift of the lasers on the Ca^+ levels and its known polarizabilities.

In general, the ac-Stark shift of an atomic state can be described by three different polarizability contributions, namely, the scalar (α_S), vector (α_V), and tensor (α_T) polarizabilities [63–65]:

$$\Delta\nu = -\frac{1}{4h}\left(\alpha_S(\omega)|E|^2 + \alpha_V(\omega)(|E_{\sigma^+}|^2 - |E_{\sigma^-}|^2)\frac{m_J}{J} + \alpha_T(\omega)\frac{(3|E_\pi|^2 - |E|^2)}{2}\frac{3m_J^2 - J(J+1)}{J(2J-1)}\right), \quad (2)$$

Where $E_\pi, E_{\sigma^+}, E_{\sigma^-}$ are the π, σ^+, σ^- polarized electrical fields, respectively, $|E|^2 = |E_\pi|^2 + |E_{\sigma^+}|^2 + |E_{\sigma^-}|^2$ is the overall electric field, m_J is the magnetic quantum number, J is the total angular momentum quantum number of the atomic state, and h is the Planck constant. The overall light shift is then calculated by the difference of the frequency shift in the excited and ground states of the driven transition.

The tensor and the vector light shift for Al^+ can be neglected, since its fine structure in the ground and excited states has zero angular momentum. Contributions from hyperfine interaction to the ac-Stark shift are small and can be neglected as well [66]. The methods for calculating the differential scalar polarizability of Al^+ are given in Appendix D.

The electric field strength of the lasers is determined by measuring the frequency shift on the $S_{1/2} \leftrightarrow D_{5/2}$ transition of Ca^+ as a function of applied laser intensity. Intensity difference between the Ca^+ and Al^+ ions, axially separated by 5.2 μm, adds only a small uncertainty on the ac-Stark shift determination (see Appendix B).

To measure the frequency shift on the Ca^+ $S_{1/2} \leftrightarrow D_{5/2}$ transition, we first pump the ion with a π pulse into the $D_{5/2}(m_{\pm1/2})$ state. Then, the $D_{5/2} \rightarrow S_{1/2}$ ($\Delta m = 0$) transition frequency is probed for different 397 nm π (σ^-) laser powers. The frequency difference between 397 nm laser on and off is a measure of the ac-Stark shift. From the known transition matrix elements [67,68], one can determine the frequency-dependent polarizabilities. With these and the measured frequency shift $\Delta\nu$, we can determine the electric field via Eq. (2) (see also Appendix C). Due to the small detuning from the $S_{1/2} \leftrightarrow P_{1/2}$ transition, the dominant frequency shift arises from coupling of the laser to the $S_{1/2}$ state, while the frequency shift of the D state is eight orders of magnitude smaller. The main uncertainty for the intensity of the 397 nm laser comes from its 4 MHz frequency uncertainty and the strongly detuning-dependent polarizability.

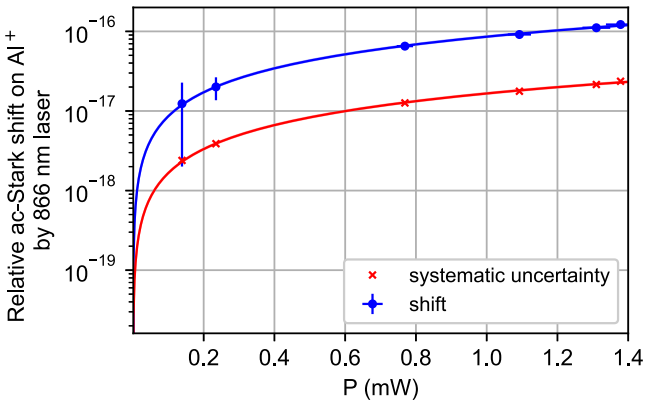


FIG. 4. Ac-Stark shift of the 866 nm laser on Al^+. The blue line shows the calculated shift, while the red line shows the uncertainty. Since we expect a linear behavior, we can extrapolate to lower powers, to estimate the value for the laser power of 17 μW used in the experiment. Here, the error bars represent the statistical error of the shift.

The frequency shift on Al^+ from the 397 nm beams is $\Delta\nu_{Al,397\sigma} = (-7.1 \pm 1.0) \times 10^{-18}$ and $\Delta\nu_{Al,397\pi} = (-0.84 \pm 0.12) \times 10^{-18}$, where the main error is due to the uncertainty in the Al^+ polarizability. One can improve the light shift measurement uncertainty by measuring the differential polarizability at 397 nm, e.g., using the method described in Ref. [69]. The uncertainty of the total ac-Stark shift on Al^+ would reduce to 3.7×10^{-19} if the uncertainty of the differential polarizability of Al^+ at 397 nm were known at the 1% level. This could be further reduced to 2×10^{-19} by stabilizing the 397 nm laser frequency to below 1 MHz.

The intensity of the repump laser can be obtained from its shift of the $S_{1/2} \leftrightarrow D_{5/2}$ transition, dominated by its coupling to the $D_{5/2}$ state. The large detuning of 4.9 THz results in a small ac-Stark shift. We use the quantum lock-in amplifier technique [70] and probe on the $S_{1/2}, m_{\pm1/2} \leftrightarrow D_{5/2}, m_{\pm5/2}$ transitions, where the 866 nm laser was switched such that the light shifts add up, and the magnetic field noise is dynamically decoupled. For this measurement, we also used different powers of the 866 nm laser to extrapolate to the low power of 17 μW used during EIT cooling. For our calculations, we assumed that we have no π polarization (since the beam propagates along the magnetic field direction). Averaging the transition frequency measurements involving the D, $m_{\pm5/2}$ states eliminates the dependence on vector light shifts and the electric field can be determined from Eq. (2) (see also Appendix C). The conversion of laser power to shift is shown in Fig. 4. The systematic uncertainty for the light shift on Al^+ is the quadratic sum of the uncertainties in the Al^+ and Ca^+ polarizabilities and the statistical uncertainty from the shift measurement. For small laser powers, the uncertainty is dominated by the shift measurement uncertainty, while for large powers it is dominated by the uncertainty of the Al^+ polarizability (see Appendix E). For the laser power used for cooling, we get a shift of $\Delta\nu_{Al,866} = (-1.37 \pm 0.27) \times 10^{-18}$. This means that we have an overall frequency shift due to the cooling and repump lasers of $\Delta\nu = (-9.3 \pm 1.1) \times 10^{-18}$, where

the main uncertainty is due to the strong 397 nm σ^- pump beam. This shift is added as a constant shift on the now time-independent second-order Doppler shift in Fig. 3. As a result, for interrogation times longer than 420 ms, continuous cooling exhibits smaller uncertainties. This threshold is dictated by the motional heating rates specific to our experimental setup and the uncertainty of the Al^+ polarizability at 397 nm.

VI. CONCLUSION

In conclusion, we have shown that simultaneous EIT cooling during clock interrogation significantly reduces time-dilation shifts and its uncertainty. The added ac-Stark shift from the cooling lasers on the clock transition has been measured to an uncertainty level of 1.0×10^{-18}, limited by the knowledge of the Al^+ polarizability at 397 nm. This allows for long interrogation times without degrading the clock's systematic frequency uncertainty. Improved calculations or measurements of the polarizability of the Al^+ clock transition for all used wavelengths with an uncertainty of 1% [69] together with improved intensity and frequency control would reduce the shift uncertainty by an order of magnitude, making it the method of choice even for interrogation times below several hundred milliseconds. The combined time-dilation and ac-Stark shifts can be further tuned by changing the EIT cooling parameters toward an optimal trade-off between steady-state $\bar{n}$ for the most relevant modes and required laser power. Using EIT cooling during clock interrogation, we demonstrated Ramsey dark times of up to 250 ms, resulting in an instability of $6.1 \times 10^{-16}/\sqrt{\tau/1\,\mathrm{s}}$ in a comparison to a Sr lattice clock, which can be extended to even longer times by phase stabilization of the probe light all the way to the ion. This paves the way for time-efficient frequency ratio measurements between different clocks at 5×10^{-18} frequency uncertainty and below, as required by the roadmap for a redefinition of the second of the International System of Units [71].

ACKNOWLEDGMENTS

We thank Daniele Nicolodi, Thomas Legero, and Uwe Sterr for providing the ultrastable Si cavity as a laser reference. We like to thank Vicent Barbé for comments on the manuscript. The project was supported by the Physikalisch-Technische Bundesanstalt, the Max-Planck Society, the Max-Planck-Riken-PTB-Center for Time, Constants and Fundamental Symmetries, and the Deutsche Forschungsgemeinschaft (DFG, German Research Foundation) under Germany's Excellence Strategy—EXC-2123 QuantumFrontiers—390837967 and Project No. 274200144—SFB 1227, Projects No. B03 and No. B02. This joint research project was financially supported by the State of Lower Saxony, Hanover, Germany, through Niedersächsisches Vorab. This project also received funding from the European Metrology Programme for Innovation and Research (EMPIR) and the European Partnership on Metrology, cofinanced by the five participating States and from the European Union's Horizon 2020 and Horizon Europe research and innovation program (Projects No. 20FUN01 TSCAC and No. 23FUN03 HIOC). This project further received funding from the European Research Council (ERC) under the European Union's Horizon 2020 research and innovation program (Grant Agreement No. 101019987). This project has been supported by the German Federal Ministry of Education and Research within the funding program "Clusters4Future," Contract No. 03ZU1209EE (QVLS-iLabs) and by the State of Lower Saxony, Hannover, Germany, through Niedersächsisches Vorab. The theoretical work has been supported in part by the U.S. Office of Naval Research Grant No. N000142512105 and by the European Research Council (ERC) under the Horizon 2020 Research and Innovation Program of the European Union (Grant Agreement No. 856415).

DATA AVAILABILITY

The data that support the findings of this article are not publicly available upon publication because it is not technically feasible and/or the cost of preparing, depositing, and hosting the data would be prohibitive within the terms of this research project. The data are available from the authors upon reasonable request.

APPENDIX A: TIME-DILATION SHIFT

The movement of the ion in the trap causes a time-dilation frequency shift [22]: $\frac{\Delta\nu}{\nu} = -\frac{\langle E_{\mathrm{kin}}\rangle}{mc^2}$. It depends on the kinetic energy E_{kin} of the ion, the mass m, and the speed of light c. The kinetic energy is given by the mean harmonicoscillator populations $\langle\bar{n}\rangle_i$ of the normal modes of motion i. For a two-ion crystal, the kinetic energy is then given by

$$E_{\mathrm{kin}} = 0.5\left(\sum_i b_i^2 \hbar\omega_i(\langle\bar{n}\rangle_i + 0.5)(1+S)\right), \tag{A1}$$

where we sum over all secular modes i and b_i is the motional mode amplitude, ω_i is the mode frequency, and S is the influence of intrinsic micromotion [72,73]. Without cooling, the motional state will increase over time due to coupling to electric field noise, which is described via the heating rate $\dot{\bar{n}}$ [37]. Assuming a linear increase in mean motional quanta, the motional phonon occupation is described by

$$\langle\bar{n}\rangle = \frac{1}{T}\int_0^T \bar{n}_0 + \dot{\bar{n}}t\,dt = \bar{n}_0 + \frac{\dot{\bar{n}}T}{2}. \tag{A2}$$

Here, $\bar{n}_0$ is the mean motional mode occupation after cooling. To minimize the frequency shift due to motion, one can cool the ion before the clock interrogation to the Doppler limit [39,44], or to the motional ground state [1,49]. Using sympathetic cooling during the clock interrogation will counteract the anomalous heating of the trap, and $\dot{\bar{n}} = 0$ in Eq. (A2). Therefore, the motional occupation depends on the cooling method used.

APPENDIX B: INTENSITY UNCERTAINTIES DUE TO ION POSITIONING

We measure the intensities of the Ca^+ cooling lasers on a single Ca^+ ion and assume the same intensities on the Al^+ to estimate their frequency shift on the clock transition. Here, we bound intensity differences between the two ions due to the beam geometry. In a two-ion crystal, the intensity of a

TABLE II. Calculated polarizabilities for the $S_{1/2}$ and $D_{5/2}$ states of Calcium for 866 nm light and 397 nm light with a detuning of +60 MHz from the $S_{1/2} \leftrightarrow P_{1/2}$ transition.

Laser	α_S	α_V	α_T
397 nm $S_{1/2}$ a.u.	$-1.55(10) \times 10^8$	$1.55(10) \times 10^8$	0
397 nm $D_{5/2}$ a.u.	4.8(1.5)	22.87(40)	3.90(51)
866 nm $S_{1/2}$ a.u.	94.8(2)	−0.30(6)	0
866 nm $D_{5/2}$ a.u.	825.9(3.4)	−1205.7(4.4)	−817.9(3.1)

laser beam on one of the two ions depends on the ordering of the ions, the spatial mode of light emitted by a fiber (here, we assume a Gaussian TEM_{00} mode), and the position and orientation of the laser beam with respect to the ion crystal's symmetry axis. Given a beam waist of 37 μm for the radial 397 nm π beam, an ion-ion separation of 5.2 μm, derived from the axial secular frequencies, and an 8.2 μm maximal axial misalignment of the beam from the center position of the two-ion crystal, we obtain an intensity difference between the two ions of 13%, which we take as the uncertainty.

For the axial 397 nm σ^- and 866 nm beams, an angle between laser beams and ion crystal axis can lead to a differential intensity between the two ions. From geometric constraints of the beam and ion-crystal tilt, we estimate a maximum angle of 9°, corresponding to an intensity difference of 3% for a 25 μm beam waist for the 397 nm σ^- and 0.7% for a 110 μm waist for the 866 nm beam. We estimate that for our parameters a worst-case displacement of the focus along the laser beam direction by the Rayleigh length leads to a difference in intensity of <0.1%.

APPENDIX C: ac-STARK SHIFT CALCULATIONS FOR CALCIUM

The scalar, vector, and tensor polarizabilities used in Eq. (2) can be calculated from the following expressions:

$$\alpha_S(\omega) = \frac{1}{2J+1} \sum_{J'} \frac{2\omega_{J'J} |\langle J \| \hat{d} \| J' \rangle|^2}{3\hbar\left(\omega_{J'J}^2 - \omega^2 - i\omega\Gamma + \Gamma_{J'}^2/4\right)} \tag{C1}$$

$$\alpha_V(\omega) = \frac{1}{2J+1} \sum_{J'} (-1)^{J+J'+1} \sqrt{\frac{6J(2J+1)}{J+1}} \times \begin{Bmatrix} 1 & 1 & 1 \\ J & J & J' \end{Bmatrix} \frac{\left(\omega + \frac{i}{2}\Gamma_{J'}\right) |\langle J \| \hat{d} \| J' \rangle|^2}{\hbar\left(\omega_{J'J}^2 - \omega^2 - i\omega\Gamma + \Gamma_{J'}^2/4\right)}, \tag{C2}$$

$$\alpha_T(\omega) = \frac{1}{2J+1} \sum_{J'} (-1)^{J+J'} \sqrt{\frac{40J(2J+1)(2J-1)}{3(J+1)(2J+3)}} \times \begin{Bmatrix} 1 & 1 & 2 \\ J & J & J' \end{Bmatrix} \frac{\omega_{J'J} |\langle J \| \hat{d} \| J' \rangle|^2}{\hbar\left(\omega_{J'J}^2 - \omega^2 - i\omega\Gamma + \Gamma_{J'}^2/4\right)}. \tag{C3}$$

Here, {} are the Wigner-6j symbols, $\omega_{JJ'}$ is the transition frequency between the states J and J', and $\langle J \| \hat{d} \| J' \rangle$ is the reduced dipole matrix element. We included an additional $\frac{1}{2J+1}$ in front to match the definition provided in Refs. [64,68], which accounts for the degeneracy of the state. $\Gamma_{J'}$ is the natural linewidth of the state J' and $\hbar$ is the reduced Planck constant. Although polarizabilities are generally complex numbers, our interest lies solely in the real part. The real part is called the dispersive part, which corresponds to a frequency shift. The imaginary part is the absorptive part and can be used to describe the photoabsorption cross section. For large detunings ($|\omega_{J'J} - \omega| \gg \Gamma/2$), the imaginary part gets small and can be neglected. In our case, we neglect the Γ terms for all transitions apart from $S_{1/2} \leftrightarrow P_{1/2}$, where we include it to first order. The calculated polarizabilities for Ca^+, used to calibrate the laser intensities in the experiment, are listed in Table II. The Wigner-6j symbols dictate a vanishing vector shift for a total angular momentum of $J = 0$, while the tensor shift is zero for $J < 1$.

The calculation of Ca^+ polarizabilities can be separated into the calculations of the ionic core contribution and a valence contribution for the scalar case. The small scalar core polarizability is essentially independent of the wavelength for the wavelengths of interest, and a static value is used. It is calculated using the random-phase approximation (RPA) [74]. The core polarizability is zero for the vector and tensor cases, since the total angular momentum is zero for the core. Valence polarizabilities are calculated using Eqs. (C1)–(C3).

We use the B-spline method to reduce infinite sums in Eqs. (C1)–(C3) to a finite number of terms. We separated the calculation of polarizability into two parts: the main term containing the first contributions from the matrix elements given in the online portal [68] and the remaining tail part. The online portal values are computed using the coupled- cluster approach and their uncertainties are estimated as described in Ref. [68]. The remaining part is computed in the Dirac-Hartree-Fock approach and corrected for RPA. The same set of B-spline orbitals is used to compute the tail as in the online portal computations to ensure consistency of the separation to the main part and the remainder term. Tail uncertainties are conservatively based on the accuracy of the DHF approach, which is on the order of 50%. The contributions to the scalar and vector polarizabilities of the 4s state at 866.45 nm in a.u. are listed in Table III. Contributions to scalar, vector, and tensor polarizabilities of the $5D_{3/2}$ state at 397.0 and 866.45 nm in a.u. are listed in Table IV.

We determine the intensity of the cooling and repump lasers on the Ca^+ ion by determining their light shifts on the S-D transition. Using Eq. (2) with the polarizability

TABLE III. Contributions to scalar and vector polarizabilities of the 4s state at 866.45 nm in a.u.

State	Matrix element	Energy	α_S	α_V
$4P_{1/2}$	2.8928(43)	25 191.51	30.77(9)	−14.09(4)
$4P_{3/2}$	4.0920(60)	25 414.4	60.74(18)	13.79(4)
$(5–12)P_{1/2}$			0.02	−0.004
$(5–12)P_{3/2}$			0.04	0.003
$(>12)P_{1/2}$			0.03(2)	−0.002 (2)
$(>12)P_{3/2}$			0.06(3)	0.001 (1)
Core			3.13(9)	
Total			94.8(2)	−0.30(6)

component X of the state Y, $\alpha_{X,Y}$, we can calculate the light shifts for the cooling lasers on the $S_{1/2}, m_J = \pm 1/2 \leftrightarrow D_{5/2}, m'_J = \pm 1/2$ ($m_J - m'_J = 0$) transition and the repump laser on the $S_{1/2}, m_J = \pm 1/2 \leftrightarrow D_{5/2}, m'_J = \pm 5/2$ ($m_J - m'_J = \pm 2$) transition:

$$\begin{aligned}
\Delta\nu_{397_\pi} &= -\frac{1}{4h}\left(\alpha_{S,D}|E|^2 + \frac{m_J}{J}\alpha_{V,D}(|E_{\sigma^+}|^2 - |E_{\sigma^-}|^2)\right. \\
&\quad \left. - \frac{4}{10}(3|E_\pi|^2 - |E|^2)\alpha_{T,D}\right) \\
&\quad - \frac{1}{4h}\left(-\alpha_{S,S}|E|^2 - \frac{m'_J}{J'}\alpha_{V,S}(|E_{\sigma^+}|^2 - |E_{\sigma^-}|^2)\right), \\
\Delta\nu_{397_\sigma} &= -\frac{1}{4h}\left(\alpha_{S,D} - \frac{1}{5}\alpha_{V,D} + \frac{2}{5}\alpha_{T,D} - \alpha_{S,S} + \alpha_{V,S}\right)|E_{\sigma^-}|^2, \\
\Delta\nu_{866} &= -\frac{1}{4h}\left(\alpha_{S,D}|E|^2 + \frac{m_J}{J}\alpha_{V,D}(|E_{\sigma^+}|^2 - |E_{\sigma^-}|^2)\right. \\
&\quad - \alpha_{T,D}\frac{|E|^2}{2} - \alpha_{S,S}|E|^2 \\
&\quad \left. - \frac{m'_J}{J'}\alpha_{V,S}(|E_{\sigma^+}|^2 - |E_{\sigma^-}|^2)\right). \qquad \text{(C4)}
\end{aligned}$$

Here, we assume a linear polarization of the 866 nm laser oriented perpendicular to the quantization axis ($E_\pi = 0$). We obtain the overall electric field by averaging the light shifts over the two measured transitions and inverting the above equations. Note that for $\Delta\nu_{866}$ and $\Delta\nu_{397_\pi}$, the averaging removes the dependence on the vector light shifts. The tensor shift component $\alpha_{T,D}$ for $\Delta\nu_{397_\pi}$ is eight orders of magnitude smaller than $\alpha_{S,S}$ (see Table II) and its effect is negligible.

APPENDIX D: ac-STARK SHIFT CALCULATIONS FOR ALUMINUM

1. Method of calculation

We consider Al^+ as a divalent ion with the core $[1s^2, 2s^2, 2p^6]$ and two valence electrons above it. The initial Dirac-Hartree-Fock self-consistency procedure included the Breit interaction and was performed for the core electrons. Then, the DHF s, p, and d orbitals with the principal quantum number $n = 3$ and 4 were constructed in the frozen-core potential. The remaining virtual orbitals were formed using a recurrent procedure described in Refs. [75,76]. In total, the basis set includes six partial waves ($l_{\max} = 5$) and orbitals with n up to 25.

In an approach combining configuration interaction (CI) and a method allowing us to include core-valence correlations [77,78], the wave functions and energy levels of the valence electrons were found by solving the multiparticle relativistic equation [77],

$$H_{\text{eff}}(E_n)\Phi_n = E_n\Phi_n, \qquad \text{(D1)}$$

where the effective Hamiltonian is defined as

$$H_{\text{eff}}(E) = H_{\text{FC}} + \Sigma(E), \qquad \text{(D2)}$$

with H_{FC} being the Hamiltonian in the frozen-core approximation. The energy-dependent operator $\Sigma(E)$ accounts for the virtual excitations of the core electrons. We constructed it in

TABLE IV. Contributions to scalar, vector, and tensor polarizabilities of the $5D_{5/2}$ state in Ca^+ at 397.0 and 866.45 nm in a.u.

Contribution	Matrix element	Energy	α_S	α_V	α_T	α_S	α_V	α_T
				397.0 nm			866.45 nm	
$4P_{3/2}$	3.283(6)$(>4P)_{3/2}$	11704	−6.18(2)	19.96(7)	6.18(2)	815.9(3.0)	−1207(4)	−815.9(3.0)
$(>4P)_{3/2}$			0.03(2)	−0.02	−0.03(2)	0.01(1)	0.0	0.0
$4F_{5/2}$	0.516(6)	54 346	0.15	−0.03	0.17	0.13	0.0	0.1
$5F_{5/2}$	0.319(2)	64 324	0.05	−0.01	0.05	0.04	0.0	0.0
$6F_{5/2}$	0.224(4)	69 747	0.02	0.00	0.02	0.02	0.0	0.0
$(>6)F_{5/2}$			0.15(7)	−0.02(1)	0.18(9)	0.14	0.0	0.2(1)
$4F_{7/2}6F_{5/2}$	2.309(25)	54 346	3.05(7)	1.51(3)	−1.09(2)	2.51(5)	0.6	−0.9
$5F_{7/2}$	1.428(8)	64 324	0.91(1)	0.38	−0.33	0.80(1)	0.2	−0.3
$6F_{7/2}$	1.000(19)	69 747	0.40(2)	0.16(1)	−0.14(1)	0.36(1)	0.1	−0.1
$7F_{7/2}$	0.755(13)	73 016	0.22(1)	0.08	−0.08	0.20(1)	0.0	−0.1
$8F_{7/2}$	0.598(9)	75 136	0.13	0.05	−0.05	0.12	0.0	0.0
$9F_{7/2}$	0.491(7)	76 589	0.09	0.03	−0.03	0.08	0.0	0.0
$10F_{7/2}$	0.412(6)	77 627	0.06	0.02	−0.02	0.05	0.0	0.0
$11F_{7/2}$	0.354(6)	78 395	0.04	0.02	−0.02	0.04	0.0	0.0
$(>11)F_{7/2}$			2.6(1.4)	0.7(4)	−0.9(5)	2.5(1.3)	0.3(2)	−0.9(4)
Core			3.02(9)			3.02(9)		
Total			4.8(1.4)	22.9(4)	3.9(5)	825.9(3.4)	−1206(4)	−817.9(3.1)

TABLE V. The ac polarizabilities of the $^1S_0$ and $^3P_0$ states of Al^+ and the differential polarizabilities $\Delta\alpha$ (in a_B^3), calculated at the wavelengths $\lambda = 397$ and 866 nm in the CI +MBPT, CI + all-order (labeled as "CI + All"), and CI + all-order + AC (labeled as "CI + All + AC") approximations, are presented. The uncertainties are given in parentheses.

		CI +MBPT	CI + All	CI + All + AC	Final
397 nm	$\alpha(^1S_0)$	29.177	29.198	29.082	29.08(12)
	$\alpha(^3P_0)$	30.285	30.309	30.232	30.23(8)
	$\Delta\alpha$	1.108	1.111	1.150	1.15(14)
866 nm	$\alpha(^1S_0)$	24.997	25.013	24.913	24.91(10)
	$\alpha(^3P_0)$	25.578	25.594	25.529	25.53(7)
	$\Delta\alpha$	0.581	0.581	0.616	0.62(12)

two ways: (1) using the second-order many-body perturbation theory (MBPT) over the residual Coulomb interaction [77] and (2) using the linearized coupled cluster single-double method [78]. In the following, we refer to these approaches as CI + MBPT and CI + all-order methods.

2. Polarizabilities

We calculated the dynamic polarizabilities of the clock $3s^2\ ^1S_0$ and $3s3p\ ^3P_0$ states and the differential polarizabilities $\Delta\alpha = \alpha(^3P_0) - \alpha(^1S_0)$ at wavelengths $\lambda = 397$ and 866 nm.

We carried out calculations in the framework of the CI + MBPT and CI + all-order methods. In both cases, the random phase approximation corrections were included. We present respective results (in a_B^3, where a_B is the Bohr radius) in the third and fourth columns of Table V.We also took into account other corrections to the electric-dipole operator: the two-particle (2P) and core Brueckner (σ) [79], the structural radiation (SR) [80,81], and the normalization (Norm.) corrections. The results of this calculation, labeled as "CI + All + AC" (where the abbreviation "AC" means all corrections beyond RPA), are displayed in the fifth column. We consider these results to be final. Based on the difference between the CI + all-order + AC and CI + all-order values, we determined the uncertainties of $\alpha(^1S_0)$ and $\alpha(^3P_0)$. The uncertainties of the final values are given in parentheses.

We also calculated the polarizabilities of the $^1S_0$ and $^3P_0$ states at the zero frequency (static) and at $\lambda = 1068$ nm. The results obtained in the CI + all-order + AC approximation are given in Table VI and compared to the experimental values.

We see that our results for $\Delta\alpha$ differ by ~20% from the central values of the experimental results of Wei *et al.* [69]. The reason for such a discrepancy is not quite clear to us. At the same time, we note that the polarizabilities of the $^1S_0$ and $^3P_0$ states are very close to each other. In differential polarizabilities, they cancel each other out at the level of 96% or more. As a result, $\Delta\alpha$ can be rather sensitive to different small corrections still not included in our calculation.

TABLE VI. The CI + all-order + AC values of the static and ac ($\lambda = 1068$ nm) polarizabilities of the $^1S_0$ and $^3P_0$ states of Al^+ and the differential polarizabilities $\Delta\alpha$ (in a_B^3) are presented.

		CI + All + AC	Experiment
Static	$\alpha(^1S_0)$	24.00	
	$\alpha(^3P_0)$	24.52	
	$\Delta\alpha$	0.52	0.43(6) [1]
			0.416(14) [69]
1068 nm	$\alpha(^1S_0)$	24.60	
	$\alpha(^3P_0)$	25.18	
	$\Delta\alpha$	0.58	0.476(14) [69]

In particular, we disregarded the quantum electrodynamical corrections. We did not take these corrections into account either for the wave functions or for the electric dipole operator. Furthermore, valence and core triple excitations were not included, and the 2P, σ, and SR corrections were calculated in the second order of perturbation theory only.

Based on this, we assume that our usual method for determining the uncertainty, as a difference between CI + all-order + AC and CI + all-order (or CI + MBPT) values, can underestimate it for differential polarizabilities. A more conservative estimate of the absolute uncertainty of the differential polarizability as

$$\Delta(\Delta\alpha) = \sqrt{(\Delta\alpha(^1S_0))^2 + (\Delta\alpha(^3P_0))^2} \tag{D3}$$

looks more reliable in the present case.

APPENDIX E: ESTIMATED FREQUENCY UNCERTAINTY OF THE ac-STARK SHIFT

Table VII shows the different contributions to the uncertainty of the light shifts. The differential polarizability of Al^+ has the most significant impact on the uncertainty, with the highest contribution coming from the 397 nm light, because it has the largest intensity. To reduce the uncertainty, a direct measurement of the differential polarizability at the cooling wavelengths should be conducted. The intensity difference between the ions is another uncertainty source due to their distance. Aligning the laser on a single ion ensures that it is well centered for the illumination of a two-ion crystal. For 397 nm, one large remaining shift is the frequency-dependent polarizability of Ca^+. Here, the error is dominated by laser frequency fluctuations, which can be overcome with a more stable frequency lock.

TABLE VII. Source of the uncertainties for all cooling and repumping lasers involved.

Effect	uncertainty 397 nm σ (10^{-18})	uncertainty 397 nm π (10^{-18})	uncertainty 866 nm (10^{-18})
$\Delta\alpha_{\mathrm{Al}}$	0.89	0.10	0.27
$\alpha_{S,S\text{-Ca}}$	0.24	0.03	0.0002
$\alpha_{V,S\text{-Ca}}$	0.24		
$\alpha_{S,D\text{-Ca}}$	$\approx 10^{-9}$	$\approx 10^{-9}$	0.004
$\alpha_{V,D\text{-Ca}}$	$\approx 10^{-10}$		
$\alpha_{T,D\text{-Ca}}$	$\approx 10^{-10}$	$\approx 10^{-9}$	0.002
extrapolation	0.09	0.008	0.015
I(Ca)/I(Al)	0.2	0.11	0.01
Total uncertainty	1.0	0.16	0.27

[1] S. M. Brewer, J.-S. Chen, A. M. Hankin, E. R. Clements, C. W. Chou, D. J. Wineland, D. B. Hume, and D. R. Leibrandt, $^{27}Al^{+}$ quantum-logic clock with a systematic uncertainty below 10^{-18}, Phys. Rev. Lett. **123**, 033201 (2019).

[2] A. Aeppli, K. Kim, W. Warfield, M. S. Safronova, and J. Ye, A clock with 8×10^{-19} systematic uncertainty, Phys. Rev. Lett. **133**, 023401 (2024).

[3] M. C. Marshall, D. A. R. Castillo, W. J. Arthur-Dworschack, A. Aeppli, K. Kim, D. Lee, W. Warfield, J. Hinrichs, N. V. Nardelli, T. M. Fortier, J. Ye, D. R. Leibrandt, and D. B. Hume, High-stability single-ion clock with 5.5×10^{-19} systematic uncertainty, Phys. Rev. Lett. **135**, 033201 (2025).

[4] K. J. Arnold, S. Bustabad, Z. Qi, Q. Qichen, Z. Zhang, Z. Zhao, and M. D. Barrett, Validating a lutetium frequency reference, J. Phys.: Conf. Ser. **2889**, 012040 (2024).

[5] W. F. McGrew, X. Zhang, R. J. Fasano, S. A. Schäffer, K. Beloy, D. Nicolodi, R. C. Brown, N. Hinkley, G. Milani, M. Schioppo, T. H. Yoon, and A. D. Ludlow, Atomic clock performance enabling geodesy below the centimetre level, Nature (London) **564**, 87 (2018).

[6] C. Sanner, N. Huntemann, R. Lange, C. Tamm, E. Peik, M. S. Safronova, and S. G. Porsev, Optical clock comparison for Lorentz symmetry testing, Nature (London) **567**, 204 (2019).

[7] M. Takamoto, I. Ushijima, N. Ohmae, T. Yahagi, K. Kokado, H. Shinkai, and H. Katori, Test of general relativity by a pair of transportable optical lattice clocks, Nat. Photon. **14**, 411 (2020).

[8] H. N. Hausser, J. Keller, T. Nordmann, N. M. Bhatt, J. Kiethe, H. Liu, I. M. Richter, M. von Boehn, J. Rahm, S. Weyers, E. Benkler, B. Lipphardt, S. Dörscher, K. Stahl, J. Klose, C. Lisdat, M. Filzinger, N. Huntemann, E. Peik, and T. E. Mehlstäubler, $^{115}In^{+}-^{172}Yb^{+}$ Coulomb crystal clock with 2.5×10^{-18} systematic uncertainty, Phys. Rev. Lett. **134**, 023201 (2025).

[9] A. Amy-Klein, E. Benkler, P. Blondé, K. Bongs, E. Cantin, C. Chardonnet, H. Denker, S. Dörscher, C.-H. Feng, J.-O. Gaudron, *et al.*, International comparison of optical frequencies with transportable optical lattice clocks, arXiv:2410.22973.

[10] K. Beloy, M. I. Bodine, T. Bothwell, S. M. Brewer, S. L. Bromley, J.-S. Chen, J.-D. Deschênes, S. A. Diddams, R. J. Fasano, T. M. Fortier, *et al.*, Frequency ratio measurements at 18-digit accuracy using an optical clock network, Nature (London) **591**, 564 (2021).

[11] T. E. Mehlstäubler, G. Grosche, C. Lisdat, P. O. Schmidt, and H. Denker, Atomic clocks for geodesy, Rep. Prog. Phys. **81**, 064401 (2018).

[12] J. Grotti, I. Nosske, S. Koller, S. Herbers, H. Denker, L. Timmen, G. Vishnyakova, G. Grosche, T. Waterholter, A. Kuhl, *et al.*, Long-distance chronometric leveling with a portable optical clock, Phys. Rev. Appl. **21**, L061001 (2024).

[13] J. Grotti, S. Koller, S. Vogt, S. Häfner, U. Sterr, C. Lisdat, H. Denker, C. Voigt, L. Timmen, A. Rolland, *et al.*, Geodesy and metrology with a transportable optical clock, Nat. Phys. **14**, 437 (2018).

[14] Y. Yuan, K. Cui, D. Liu, J. Yuan, J. Cao, D. Wang, S. Chao, H. Shu, and X. Huang, Demonstration of chronometric leveling using transportable optical clocks beyond laser coherence limit, Phys. Rev. Appl. **21**, 044052 (2024).

[15] R. M. Godun, P. B. R. Nisbet-Jones, J. M. Jones, S. A. King, L. A. M. Johnson, H. S. Margolis, K. Szymaniec, S. N. Lea, K. Bongs, and P. Gill, Frequency ratio of two optical clock transitions in $^{171}Yb^{+}$ and constraints on the time variation of fundamental constants, Phys. Rev. Lett. **113**, 210801 (2014).

[16] M. S. Safronova, The search for variation of fundamental constants with clocks, Ann. Phys. **531**, 1800364 (2019).

[17] N. Sherrill, A. O. Parsons, C. F. A. Baynham, W. Bowden, E. A. Curtis, R. Hendricks, I. R. Hill, R. Hobson, H. S. Margolis, B. I. Robertson, M. Schioppo, K. Szymaniec, A. Tofful, J. Tunesi, R. M. Godun, and X. Calmet, Analysis of atomic-clock data to constrain variations of fundamental constants, New J. Phys. **25**, 093012 (2023).

[18] M. Filzinger, A. R. Caddell, D. Jani, M. Steinel, L. Giani, N. Huntemann, and B. M. Roberts, Ultralight dark matter search with space-time separated atomic clocks and cavities Phys. Rev. Lett. **134**, 031001 (2025).

[19] B. M. Roberts, P. Delva, A. Al-Masoudi, A. Amy-Klein, C. Bærentsen, C. F. A. Baynham, E. Benkler, S. Bilicki, S. Bize, W. Bowden, *et al.*, Search for transient variations of the fine structure constant and dark matter using fiber-linked optical atomic clocks, New J. Phys. **22**, 093010 (2020).

[20] M. Filzinger, S. Dörscher, R. Lange, J. Klose, M. Steinel, E. Benkler, E. Peik, C. Lisdat, and N. Huntemann, Improved limits on the coupling of ultralight bosonic dark matter to photons from optical atomic clock comparisons, Phys. Rev. Lett. **130**, 253001 (2023).

[21] C.-H. Yeh, K. C. Grensemann, L. S. Dreissen, H. A. Fürst, and T. E. Mehlstäubler, Robust and scalable rf spectroscopy in first-order magnetic sensitive states at second-long coherence time, New J. Phys. **25**, 093054 (2023).

[22] A. D. Ludlow, M. M. Boyd, J. Ye, E. Peik, and P. O. Schmidt, Optical atomic clocks, Rev. Mod. Phys. **87**, 637 (2015).

[23] W. M. Itano, J. C. Bergquist, J. J. Bollinger, J. M. Gilligan, D. J. Heinzen, F. L. Moore, M. G. Raizen, and D. J. Wineland, Quantum projection noise: Population fluctuations in two-level systems, Phys. Rev. A **47**, 3554 (1993).

[24] E. Peik, T. Schneider, and C. Tamm, Laser frequency stabilization to a single ion, J. Phys. B: At. Mol. Opt. Phys. **39**, 145 (2006).

[25] F. Riehle, *Frequency Standards: Basics and Applications* (Wiley-VCH, Weinheim, 2004).

[26] K. Pyka, N. Herschbach, J. Keller, and T. E. Mehlstäubler, A high-precision segmented Paul trap with minimized micromotion for an optical multiple-ion clock, Appl. Phys. B **114**, 231 (2014).

[27] J. Keller, T. Burgermeister, D. Kalincev, J. Kiethe, and T. E. Mehlstäubler, Evaluation of trap-induced systematic frequency shifts for a multi-ion optical clock at the 10^{-19} level, J. Phys.: Conf. Ser. **723**, 012027 (2016).

[28] T. R. Tan, R. Kaewuam, K. J. Arnold, S. R. Chanu, Z. Zhang, M. S. Safronova, and M. D. Barrett, Suppressing inhomogeneous broadening in a lutetium multi-ion optical clock, Phys. Rev. Lett. **123**, 063201 (2019).

[29] L. Pelzer, K. Dietze, V. J. Martínez-Lahuerta, L. Krinner, J. Kramer, F. Dawel, N. C. H. Spethmann, K. Hammerer, and P. O. Schmidt, Multi-ion frequency reference using dynamical decoupling, Phys. Rev. Lett. **133**, 033203 (2024).

[30] N. Akerman and R. Ozeri, Operating a multi-ion clock with dynamical decoupling, Phys. Rev. Lett. **134**, 013201 (2025).

[31] I. D. Leroux, N. Scharnhorst, S. Hannig, J. Kramer, L. Pelzer, M. Stepanova, and P. O. Schmidt, On-line estimation of local oscillator noise and optimisation of servo parameters in atomic clocks, Metrologia **54**, 307 (2017).

[32] D. G. Matei, T. Legero, S. Häfner, C. Grebing, R. Weyrich, W. Zhang, L. Sonderhouse, J. M. Robinson, J. Ye, F. Riehle, and U. Sterr, 1.5 µm lasers with sub-10 mHz linewidth, Phys. Rev. Lett. **118**, 263202 (2017).

[33] S. Dörscher, A. Al-Masoudi, M. Bober, R. Schwarz, R. Hobson, U. Sterr, and C. Lisdat, Dynamical decoupling of laser phase noise in compound atomic clocks, Commun. Phys. **3**, 185 (2020).

[34] T. Rosenband and D. R. Leibrandt, Exponential scaling of clock stability with atom number, arXiv:1303.6357.

[35] J. Borregaard and A. S. Sørensen, Efficient atomic clocks operated with several atomic ensembles, Phys. Rev. Lett. **111**, 090802 (2013).

[36] V. J. Martínez-Lahuerta, S. Eilers, T. E. Mehlstäubler, P. O. Schmidt, and K. Hammerer, *Ab initio* quantum theory of mass defect and time dilation in trapped-ion optical clocks, Phys. Rev. A **106**, 032803 (2022).

[37] M. Brownnutt, M. Kumph, P. Rabl, and R. Blatt, Ion-trap measurements of electric-field noise near surfaces, Rev. Mod. Phys. **87**, 1419 (2015).

[38] M. Zeng, Y. Huang, B. Zhang, Y. Hao, Z. Ma, R. Hu, H. Zhang, Z. Chen, M. Wang, H. Guan, and K. Gao, Toward a transportable Ca^+ optical clock with a systematic uncertainty of 4.8×10^{-18}, Phys. Rev. Appl. **19**, 064004 (2023).

[39] N. Huntemann, C. Sanner, B. Lipphardt, Chr. Tamm, and E. Peik, Single-ion atomic clock with 3×10^{-18} systematic uncertainty, Phys. Rev. Lett. **116**, 063001 (2016).

[40] Z. Y. Ma, K. Deng, Z. Y. Wang, W. Z. Wei, P. Hao, H. X. Zhang, L. R. Pang, B. Wang, F. F. Wu, H. L. Liu, W. H. Yuan, J. L. Chang, J. X. Zhang, Q. Y. Wu, J. Zhang, and Z. H. Lu, Quantum-logic-based $^{25}Mg^+$ - $^{27}Al^+$ optical frequency standard for the redefinition of the SI second, Phys. Rev. Appl. **21**, 044017 (2024).

[41] T. Rosenband, D. B. Hume, P. O. Schmidt, C. W. Chou, A. Brusch, L. Lorini, W. H. Oskay, R. E. Drullinger, T. M. Fortier, J. E. Stalnaker, S. A. Diddams, W. C. Swann, N. R. Newbury, W. M. Itano, D. J. Wineland, and J. C. Bergquist, Frequency ratio of Al^+ and Hg^+ single-ion optical clocks; metrology at the 17^{th} decimal place, Science **319**, 1808 (2008).

[42] Z. Zhiqiang, K. J. Arnold, R. Kaewuam, and M. D. Barrett, $^{176}Lu^+$ clock comparison at the 10^{-18} level via correlation spectroscopy, Sci. Adv. **9**, eadg1971 (2023).

[43] C. W. Chou, D. B. Hume, J. C. J. Koelemeij, D. J. Wineland, and T. Rosenband, Frequency comparison of two high-accuracy Al^+ optical clocks, Phys. Rev. Lett. **104**, 070802 (2010).

[44] K. Cui, S. Chao, C. Sun, S. Wang, P. Zhang, Y. Wei, J. Yuan, J. Cao, H. Shu, and X. Huang, Evaluation of the systematic shifts of a $^{40}Ca^+$ - $^{27}Al^+$ optical clock, Eur. Phys. J. D **76**, 140 (2022).

[45] C. F. Roos, D. Leibfried, A. Mundt, F. Schmidt-Kaler, J. Eschner, and R. Blatt, Experimental demonstration of ground state laser cooling with electromagnetically induced transparency, Phys. Rev. Lett. **85**, 5547 (2000).

[46] R. Lechner, C. Maier, C. Hempel, P. Jurcevic, B. P. Lanyon, T. Monz, M. Brownnutt, R. Blatt, and C. F. Roos, Electromagnetically-induced-transparency ground-state cooling of long ion strings, Phys. Rev. A **93**, 053401 (2016).

[47] N. Scharnhorst, J. Cerrillo, J. Kramer, I. D. Leroux, J. B. Wübbena, A. Retzker, and P. O. Schmidt, Experimental and theoretical investigation of a multimode cooling scheme using multiple electromagnetically-induced-transparency resonances, Phys. Rev. A **98**, 023424 (2018).

[48] C. Sun, K. Cui, S. Chao, Y. Wei, J. Yuan, J. Cao, H. Shu, and X. Huang, Sympathetic electromagnetically induced transparency ground state cooling of a $^{40}Ca^+ - ^{27}Al^+$ pair in an $^{27}Al^+$ clock, Chin. Phys. B **32**, 050601 (2023).

[49] J.-S. Chen, S. M. Brewer, C. W. Chou, D. J. Wineland, D. R. Leibrandt, and D. B. Hume, Sympathetic ground state cooling and time-dilation shifts in an $^{27}Al^+$ optical clock, Phys. Rev. Lett. **118**, 053002 (2017).

[50] J. A. Kramer, An aluminum optical clock setup and its evaluation using Ca_+, Ph.D. thesis, Leibniz Universität Hannover, 2023.

[51] A. M. Hankin, E. R. Clements, Y. Huang, S. M. Brewer, J.-S. Chen, C. W. Chou, D. B. Hume, and D. R. Leibrandt, Systematic uncertainty due to background-gas collisions in trapped-ion optical clocks, Phys. Rev. A **100**, 033419 (2019).

[52] G. Morigi, J. Eschner, and C. H. Keitel, Ground state laser cooling using electromagnetically induced transparency, Phys. Rev. Lett. **85**, 4458 (2000).

[53] D. Hume, T. Rosenband, and D. Wineland, High-fidelity adaptive qubit detection through repetitive quantum nondemolition measurements, Phys. Rev. Lett. **99**, 120502 (2007).

[54] S. Amairi, A long optical cavity for sub-hertz laser spectroscopy, Ph.D. thesis, Leibniz Universität Hannover, 2014.

[55] N. Scharnhorst, J. B. Wübbena, S. Hannig, K. Jakobsen, J. Kramer, I. D. Leroux, and P. O. Schmidt, High-bandwidth transfer of phase stability through a fiber frequency comb, Opt. Express **23**, 19771 (2015).

[56] E. Benkler, B. Lipphardt, T. Puppe, R. Wilk, F. Rohde, and U. Sterr, End-to-end topology for fiber comb based optical frequency transfer at the 10^{-21} level, Opt. Express **27**, 36886 (2019).

[57] J. Ye, J.-L. Peng, R. J. Jones, K. W. Holman, J. L. Hall, D. J. Jones, S. A. Diddams, J. Kitching, S. Bize, J. C. Bergquist, L. W. Hollberg, L. Robertsson, and L.-S. Ma, Delivery of high-stability optical and microwave frequency standards over an optical fiber network, J. Opt. Soc. Am. B **20**, 1459 (2003).

[58] B. Kraus, F. Dawel, S. Hannig, J. Kramer, C. Nauk, and P. O. Schmidt, Phase-stabilized UV light at 267 nm through twofold second harmonic generation, Opt. Express **30**, 44992 (2022).

[59] Y. Colombe, D. H. Slichter, A. C. Wilson, D. Leibfried, and D. J. Wineland, Single-mode optical fiber for high-power, low-loss UV transmission, Opt. Express **22**, 19783 (2014).

[60] C. D. Marciniak, H. B. Ball, A. T.-H. Hung, and M. J. Biercuk, Towards fully commercial, UV-compatible fiber patch cords, Opt. Express **25**, 15643 (2017).

[61] R. Schwarz, A cryogenic strontium lattice clock, Doctoral thesis, Institutionelles Repositorium der Leibniz Universität Hannover, Hannover, 2022.

[62] A. J. Rasmusson, M. D'Onofrio, Y. Xie, J. Cui, and P. Richerme, Optimized pulsed sideband cooling and enhanced thermometry of trapped ions, Phys. Rev. A **104**, 043108 (2021).

[63] D. A. Steck, Quantum and Atom Optics, http://steck.us/teaching.

[64] K. D. Bonin and V. V. Kresin, *Electric-Dipole Polarizabilities of Atoms, Molecules, and Clusters* (World Scientific, Singapore, 1997).

[65] D. R. Dounas-Frazer, K. Tsigutkin, A. Family, and D. Budker, Measurement of dynamic Stark polarizabilities by analyzing spectral line shapes of forbidden transitions, Phys. Rev. A **82**, 062507 (2010).

[66] C. Shi, J.-L. Robyr, U. Eismann, M. Zawada, L. Lorini, R. L. Targat, and J. Lodewyck, Polarizabilities of the ^{87}Sr clock transition, Phys. Rev. A **92**, 012516 (2015).

[67] M. Hettrich, T. Ruster, H. Kaufmann, C. F. Roos, C. T. Schmiegelow, F. Schmidt-Kaler, and U. G. Poschinger, Measurement of dipole matrix elements with a single trapped ion, Phys. Rev. Lett. **115**, 143003 (2015).

[68] A. Kiruga, C. Cheung, D. Filin, P. Barakhshan, A. Bhosale, V. Badhan, B. Arora, R. Eigenmann, and M. S. Safronova, Portal for high-precision atomic data and computation, arXiv:2506.08170.

[69] Y.-F. Wei, S.-J. Chao, K.-F. Cui, C.-B. Li, S.-C. Yu, H. Zhang, H.-L. Shu, J. Cao, and X.-R. Huang, Improved measurement of the differential polarizability using co-trapped ions, Phys. Rev. Lett. **133**, 033001 (2024).

[70] S. Kotler, N. Akerman, Y. Glickman, A. Keselman, and R. Ozeri, Single-ion quantum lock-in amplifier, Nature (London) **473**, 61 (2011).

[71] N. Dimarcq, M. Gertsvolf, G. Mileti, S. Bize, C. W. Oates, E. Peik, D. Calonico, T. Ido, P. Tavella, F. Meynadier, *et al.*, Roadmap towards the redefinition of the second, Metrologia **61**, 012001 (2024).

[72] J. B. Wübbena, S. Amairi, O. Mandel, and P. O. Schmidt, Sympathetic cooling of mixed-species two-ion crystals for precision spectroscopy, Phys. Rev. A **85**, 043412 (2012).

[73] D. J. Berkeland, J. D. Miller, J. C. Bergquist, W. M. Itano, and D. J. Wineland, Minimization of ion micromotion in a Paul trap, J. Appl. Phys. **83**, 5025 (1998).

[74] B. Arora, M. S. Safronova, and C. W. Clark, Blackbody-radiation shift in a $^{43}Ca^{+}$ ion optical frequency standard, Phys. Rev. A **76**, 064501 (2007).

[75] M. G. Kozlov, S. G. Porsev, and V. V. Flambaum, Manifestation of the nuclear anapole moment in the M1 transitions in bismuth, J. Phys. B: At. Mol. Opt. Phys. **29**, 689 (1996).

[76] M. G. Kozlov, S. G. Porsev, M. S. Safronova, and I. I. Tupitsyn, Ci-mbpt: A package of programs for relativistic atomic calculations based on a method combining configuration interaction and many-body perturbation theory, Comput. Phys. Commun. **195**, 199 (2015).

[77] V. A. Dzuba, V. V. Flambaum, and M. G. Kozlov, Combination of the many-body perturbation theory with the configuration-interaction method, Phys. Rev. A **54**, 3948 (1996).

[78] M. S. Safronova, M. G. Kozlov, W. R. Johnson, and D. Jiang, Development of a configuration-interaction plus all-order method for atomic calculations, Phys. Rev. A **80**, 012516 (2009).

[79] V. A. Dzuba, M. G. Kozlov, S. G. Porsev, and V. V. Flambaum, Using effective operators in calculating the hyperfine structure of atoms, J. Exp. Theor. Phys. **87**, 885 (1998).

[80] V. A. Dzuba, V. V. Flambaum, P. G. Silvestrov, and O. P. Sushkov, Correlation potential method for the calculation of energy levels, hyperfine structure and E1 transition amplitudes in atoms with one unpaired electron, J. Phys. B **20**, 1399 (1987).

[81] S. A. Blundell, W. R. Johnson, Z. W. Liu, and J. Sapirstein, Relativistic all-order calculations of energies and matrix elements for Li and Be^{+}, Phys. Rev. A **40**, 2233 (1989).